Supplementary material to First-Order Phase Transition of the Schwinger Model with a Quantum Computer

Takis Angelides [1,2,*] Pranay Naredi [3] Arianna Crippa [1,2] Karl Jansen [2,3] Stefan Kühn [2] Ivano Tavernelli [4] and Derek S. Wang [5]

[1] *Institut für Physik, Humboldt-Universität zu Berlin, Newtonstr. 15, 12489 Berlin, Germany*
[2] *CQTA, Deutsches Elektronen-Synchrotron DESY, Platanenallee 6, 15738 Zeuthen, Germany*
[3] *Computation-Based Science and Technology Research Center, The Cyprus Institute, 20 Kavafi Street, 2121 Nicosia, Cyprus*
[4] *IBM Research Europe - Zurich, Säumerstrasse 4, 8803 Rüschlikon, Switzerland*
[5] *IBM Quantum, IBM T.J. Watson Research Center, Yorktown Heights, NY 10598, USA*

(Dated: August 13, 2024)

I. DERIVATION OF THE HAMILTONIAN

In this section we derive the Hamiltonian for Wilson fermions, in particular, we provide the details of the fermion ordering chosen. Subsequently, we show the Jordan Wigner transformation and the final Hamiltonians in spin formulation used in the simulations for both Wilson and staggered fermions.

We turn first to Wilson fermions starting from the free Dirac Hamiltonian on the lattice which is given by

$$H = a \sum_n \psi_n^\dagger \gamma^0 \left(-i\gamma^1 \partial_1 + m_{\text{lat}} \right) \psi_n, \tag{1}$$

with a the lattice spacing, n specifying the lattice site and m_{lat} the lattice mass. The derivative $\partial_1 \psi_n$ appearing in the above corresponds to the symmetric finite differences $(\psi_{n+1} - \psi_{n-1})/2a$. We add the Wilson term [1, 2],

$$\begin{aligned} \Delta H_W &= -r \frac{a^2}{2} \sum_n \overline{\psi}_n \left(\partial_1\right)^2 \psi_n \\ &= -r \frac{a^2}{2} \sum_n \overline{\psi}_n \left(\frac{\psi_{n+1} + \psi_{n-1} - 2\psi_n}{a^2} \right), \end{aligned} \tag{2}$$

to H, where we have used the spatial discrete symmetrized second derivative for $(\partial_1)^2$ and the Wilson parameter r. For the γ matrices we make the choice $\gamma^0 = X$, $\gamma^1 = iZ$, with X, Z, being the standard Pauli matrices. To ensure invariance under local symmetry transformations, we have to introduce the link operators U_n, and its canonical conjugate the electric field operator $E_n = gL_n$, with g being the coupling between fermions and bosons. The resulting gauge invariant Hamiltonian reads

$$\begin{aligned} H_W = \sum_n \Bigg(& -\overline{\psi}_n \left(\frac{r + i\gamma^1}{2} \right) U_n \psi_{n+1} \\ & + \overline{\psi}_n \left(\frac{-r + i\gamma^1}{2} \right) U_n^\dagger \psi_{n-1} \\ & + (am_{\text{lat}} + r) \overline{\psi}_n \psi_n + \frac{a}{2} \left(E_n + \frac{g\theta}{2\pi} \right)^2 \Bigg), \end{aligned} \tag{3}$$

where we explicitly consider the background electric field $g\theta/2\pi$. The gauge invariant states have to fulfill Gauss's law, $L_n - L_{n-1} = Q_n$, with the charge operator given by $Q_n = a\psi_n^\dagger \psi_n - 1$. For open boundary conditions, this expression can be solved iteratively, where we find $L_n = \varepsilon_0 + \sum_{k=0}^{n} Q_k$ with ε_0 the electric field on the left boundary. Similar to the main text, we consider here $\varepsilon_0 = 0$. Substituting this into the Hamiltonian and applying the unitary transformation from Ref. [3], we can fully remove the gauge fields. For numerical calculations, it is convenient to make the fields ψ dimensionless with $\phi_{n,\alpha} = (-1)^n \sqrt{a} \psi_{n,\alpha}$, where the index $\alpha \in \{1, 2\}$ specifies the spinor component. We also make the Hamiltonian dimensionless by rescaling it to $\tilde{W} = 2H/ag^2$. Contrary to Refs. [1, 2], we additionally apply the transformation $\phi_{n,\alpha} \to (-1)^n (-i)^\alpha \phi_{n,\alpha}$ to the fermionic fields, which results in a completely real Hamiltonian.

In order translate the fermionic fields to qubits, we choose to map the spinor $\phi_{n,\alpha}$ linearly using the following mapping $\phi_{n,\alpha} \to \chi_{2n - \lfloor \frac{\alpha}{2} \rfloor + 1}$. Now we can apply a Jordan-Wigner transformation [4], $\chi_n = \prod_{k<n} (iZ_k) \sigma_n^-$. The charge operator after this transformation becomes $Q_n = (Z_{2n} + Z_{2n+1})/2$, with $n \in \{0, N-1\}$. To enforce vanishing total charge, in case it is needed, we use a penalty term Λ to the Hamiltonian, $W_W = \tilde{W} + \Lambda$, where $\Lambda = \lambda \left(\sum_{n=0}^{N-1} Q_n \right)^2$. Provided λ is chosen large enough, we can ensure we remain in the sector with vanishing total charge. A few algebraic manipulations on

* takis.angelides@desy.de

nested sums then results in the final Hamiltonian

$$
\begin{aligned}
W_W = & x(r-1)\sum_{n=0}^{N-2}\left(\sigma_{2n}^{+}Z_{2n+1}Z_{2n+2}\sigma_{2n+3}^{-}+\text{h.c.}\right)\\
& + \frac{x(r+1)}{2}\sum_{n=0}^{N-2}\left(X_{2n+1}X_{2n+2}+Y_{2n+1}Y_{2n+2}\right)\\
& + \left(\frac{m_{\text{lat}}}{g}\sqrt{x}+xr\right)\sum_{n=0}^{N-1}\left(X_{2n}X_{2n+1}+Y_{2n}Y_{2n+1}\right)\\
& + \frac{1}{2}\sum_{n=0}^{2N-1}\sum_{k=n+1}^{2N-1}\left(N-\left\lceil\frac{k+1}{2}\right\rceil+\lambda\right)Z_nZ_k \qquad (4)\\
& + l_0\sum_{n=0}^{2N-3}\left(N-\left\lceil\frac{n+1}{2}\right\rceil\right)Z_n\\
& + l_0^2(N-1)+\frac{1}{4}N(N-1)+\frac{\lambda N}{2},
\end{aligned}
$$

where $\lceil\cdot\rceil$ is the ceiling function to the nearest integer greater than the input.

For the staggered case, we directly apply the Jordan-Wigner transformation to Eq. (16) of the main text and set $\phi_n = \prod_{k<n}(iZ_k)\sigma_n^-$. Similar to the Wilson case, we add the penalty term to restrict the Hamiltonian to the subspace of vanishing total charge. After the Jordan-Wigner transformation, for staggered fermions, the charge operator becomes $Q_n = (Z_n + (-1)^n)/2$ and the final Hamiltonian including the penalty term is given by

$$
\begin{aligned}
W_S = & \frac{x}{2}\sum_{n=0}^{N-2}\left(X_nX_{n+1}+Y_nY_{n+1}\right)\\
& + \frac{1}{2}\sum_{n=0}^{N-2}\sum_{k=n+1}^{N-1}(N-k-1+\lambda)Z_nZ_k\\
& + \sum_{n=0}^{N-2}\left(\frac{N}{4}-\frac{1}{2}\left\lceil\frac{n}{2}\right\rceil+l_0(N-n-1)\right)Z_n \qquad (5)\\
& + \frac{m_{\text{lat}}}{g}\sqrt{x}\sum_{n=0}^{N-1}(-1)^nZ_n\\
& + l_0^2(N-1)+\frac{1}{2}l_0N+\frac{1}{8}N^2+\frac{\lambda}{4}N.
\end{aligned}
$$

II. ZERO NOISE EXTRAPOLATIONS

Here we discuss the technical details of the ZNE that we used for our inference runs. In our implementation, global folding was applied with noise factors 1, 3, and 5, with 10,000 shots collected from each circuit. The noise factors are defined as follows: if the circuit is represented by the unitary U, then at noise factor f, where f is an odd number, a total of $(f-1)/2$ pairs of unitaries $U^\dagger U$ is added to the circuit. For example, noise factor 3, the circuit would be $U(U^\dagger U)$ and at noise factor 5 it would be $U(U^\dagger U)(U^\dagger U)$.

To get a final zero-noise extrapolated expectation value, we first compute preliminary zero-noise extrapolated values using three approaches: a linear fit to noise factors 1, 3, and 5; a linear fit to noise factors 1 and 3; and a second-order polynomial fit to noise factors 1, 3, and 5. We then calculate the final zero-noise extrapolated value as a weighted average of the preliminary values, weighted according to their variance. Their variance emanates from the fitting procedure performed on points which themselves have a variance. Each point within a fit, i.e. each point at a given noise factor, is the average of the 10 twirls used from the Pauli twirling error mitigation technique described in the main text. Hence, the corresponding error on each point within a fit comes from this average. The error of each one of these 10 twirls before twirl averaging is taken to be the square root of the ratio of the variance of the measurement divided by the number of shots.

In Fig. 1 we show specific parameter examples of the ZNE fits. We present representative cases for both situations, where the ZNE was able to improve the expectation value of the observable to be measured and where it was not.

III. TENSOR NETWORKS

In order to find an MPS approximation for the ground states of the two Hamiltonians we consider, we use the two-site variational ground state search algorithm from the ITensors library [5]. The number of iterations was fixed to 500 and the tolerance η for the relative change in energy between two sweeps was set to 10^{-9}, which in turn gives an approximation for the error on the electric field density given by the value of the electric field density multiplied by $\sqrt{\eta}$ [6]. Additionally, we restrict the MPS to the sector of vanishing total charge by applying the symmetry directly to the ansatz [7], thus no penalty term is used in the spin Hamiltonians.

In order to compare between the Wilson and staggered fermion discretization approaches, we carry out a continuum limit extrapolation. This implies following lines of constant physics in the physical phase space, which requires the calculation of the mass shift for each N, x, l_0. With our work confined to a fixed volume of $N/\sqrt{x} = 30$, this necessitates the determination of the mass shift for individual values of N and l_0 only. In this work, we followed the method based on the electric field density introduced in Ref. [1]. Table I quantifies the effect of not accounting for an l_0 dependence on the mass shift with staggered fermions. Finally, Fig. 2 is qualitatively showing the effect of not accounting for the mass shift when using Wilson fermions, which was also observed in [1]. The bond dimension for all MPS data was set to $D = 20, 40, 60, 80$ and we then extrapolate the last 3 points to infinite D in the electric field density against

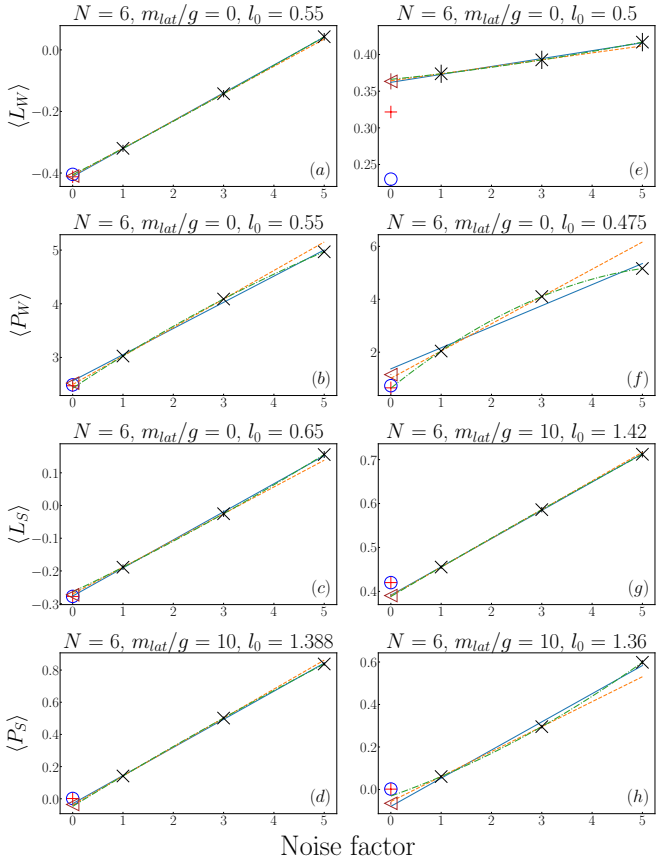

Supplementary Figure 1. Electric field density $\langle L_{W,S} \rangle$ and particle number $\langle P_{W,S} \rangle$ against noise factor for zero noise extrapolations (ZNE) on the data (black crosses) obtained from quantum hardware for different parameters specified in the titles of each subplot with Wilson and staggered fermions. The red pluses are noiseless values of the observables and the blue circles are the exact diagonalization results. For the fits we fit a first-order polynomial to either all points (blue continuous line) or to points with noise factor 1, 3 (dashed orange line). We also fit a second order polynomial to all points (green dotted dashed line). The brown triangle is the weighted average of the extrapolated points of these 3 fits. The plots on the left $(a-d)$ are showing examples where the ZNE helped take the expectation values measured closer to the noiseless result, while on the right $(e-h)$ we show occasions where the ZNE might not be able to improve the result. However, overall the results of the main text indicate that ZNE can significantly improve the results. The calculation of the error bars is described within this Appendix and where they are not visible, they are smaller than the markers and y-scale.

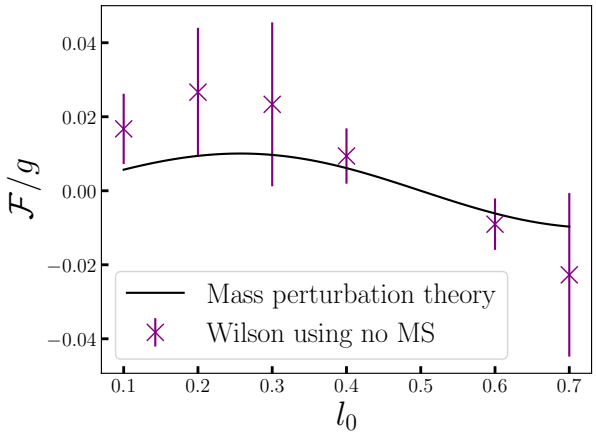

Supplementary Figure 2. Electric field density $\mathcal{F}/g$ against l_0 for Wilson fermions using no mass shift at $m_r/g = m_{\rm lat}/g = 0.01$. The MSE is calculated as in the main text and found here to be $7.939 \cdot 10^{-4}$. The error bars emanate from the errors in the variational algorithm to compute the relevant ground states, the extrapolation in bond dimension and in lattice spacing.

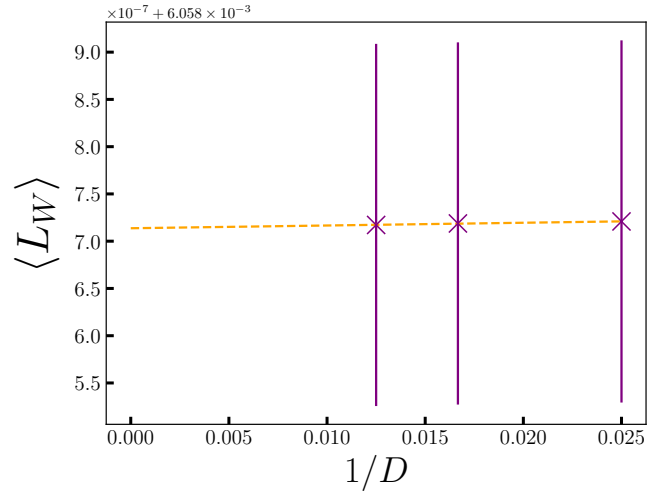

Supplementary Figure 3. Electric field density $\langle L_W \rangle$ against inverse bond dimension $1/D$ to extrapolate to $D \to \infty$ with $D = 40, 60, 80$. This example is for Wilson fermions at $N = 100$, $l_0 = 0.1$, $m_{\rm lat}/g = -0.08236266$. Similar behavior was observed for staggered fermions as well. The error bars are emanating from the variational algorithm to compute the relevant ground states.

$1/D$ plot as shown in Fig. 3. The central value is taken to be the average of the extrapolated value of the linear fit and the electric field density value at the highest D calculated, while the error is approximated to be half the difference between these values. The smaller D solutions were given as initial ansatz to the higher D, while $D = 20$ was initialized with a random MPS.

After calculating the mass shift, we proceed with the calculation of the electric field density for a fixed renormalized mass of $m_r/g = 0.01$ and for different values of l_0. This procedure enables the comparison of our continuum extrapolation quantities with the theoretical results from mass perturbation theory [8]. We use N from 70 to 100 in steps of 10, which in turn determines the $ag = 1/\sqrt{x}$ values through the fixed volume. After bond dimension extrapolations of electric field density, we extrapolate this observable to $ag = 0$ as shown in Fig. 4.

Performance analysis of continuum extrapolations with matrix product states

l_0	0.1	0.2	0.3	0.4	0.6	0.7
Wilson	4.45001467e-05	1.00338853e-05	5.58001106e-05	3.04735487e-05	3.64867975e-05	2.17138610e-05
Staggered (MS_t, same num. qubits as Wilson)}	0.00012783	0.00016672	0.00022494	0.0003207	0.00045197	0.00046271
Staggered (MS_L, same x as Wilson)	6.97181950e-06	4.86364083e-06	1.14145910e-05	4.21571198e-05	5.52293937e-05	3.33572489e-05
Staggered (MS_t, same x as Wilson)	2.91080596e-04	2.63562909e-04	8.61951831e-05	1.03764598e-04	6.79235186e-04	6.37947680e-04
Staggered (MS_L, same num. qubits as Wilson)	2.05654489e-05	1.75062880e-05	1.54209990e-05	1.40152738e-04	5.40892433e-05	5.13089222e-05

TABLE I. This table corresponds to the absolute error with respect to the results from mass perturbation theory for the data presented in the main text. For staggered fermions that use the theoretically predicted mass shift, MS_t, the error tends to grow with l_0 due to the fact that the MS_t does not account for an l_0 dependence.

For the Wilson case, we take the extrapolated value of the linear fit and assign an approximated error to it which is taken to be the difference between that value and the extrapolated value of a quadratic fit. For the staggered case, it was observed that second-order polynomial fits were more suitable and that they converge faster to the continuum; therefore we keep the extrapolated value of the quadratic fit and again approximate the error as in the Wilson case. To avoid boundary effects, the electric field density for Wilson fermions is measured using the middle link, and for staggered fermions, the four middle links are measured to also reduce the staggering effect.

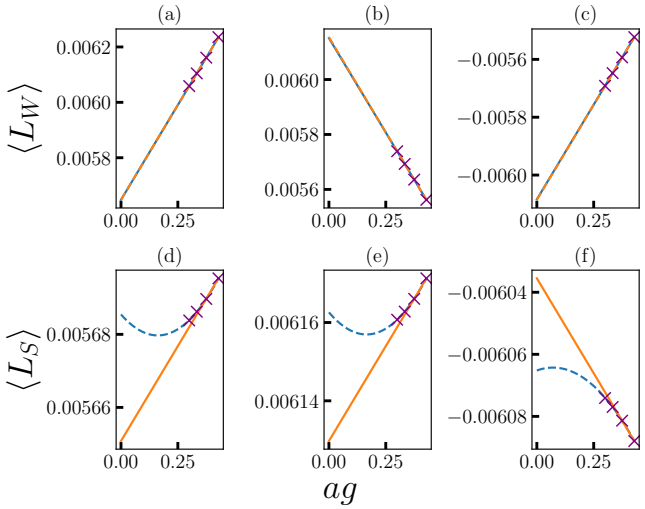

Supplementary Figure 4. Electric field density $\langle L_{W,S} \rangle$ against ag to extrapolate to the continuum limit with fixed volume $N/\sqrt{x} = 30$, fixed $m_\mathrm{r}/g = 0.01$, using $N = 70, 80, 90, 100$. The continuous orange line is a linear fit and the dashed blue line is a second order polynomial fit. $(a-c)$ is showing Wilson fermions for $l_0 = 0.1, 0.4, 0.6$ respectively and $(d-f)$ the same for staggered fermions with the same x as Wilson fermions and the electric field density method for the mass shift [1]. The error bars emanate from the variational algorithm to compute the relevant ground states and the extrapolation in bond dimension. They are much smaller than the markers and thus, are not visible.

IV. LATTICE EFFECTS ON THE PHASE TRANSITION

Here we derive an analytical expression for the location of the first-order phase transition of the lattice Schwinger model focusing on the case of $m/g >> 1$, i.e. the limit where the kinetic term is negligible.

We start by mapping the electric field energy to its lattice version. The electric field operator can also be made dimensionless using the coupling g between the fermions and gauge fields, i.e. $E \to gL_n$. The mapping from a continuum theory electric field energy to the corresponding lattice version is

$$\int_{-\infty}^{\infty} \frac{E^2}{2} dx \to a \sum_{n=0}^{N-2} \frac{g^2 L_n^2}{2}. \tag{6}$$

Our derivation will not depend on the specific lattice fermion formulation, hence the result can be seen as general and applying to both Wilson and staggered formulations. The key ingredient is the fact that at the point of the first-order phase transition, which we label with l_0^*, the ground state is two-fold degenerate.

On the left of the phase transition ($l_0 < l_0^*$), the ground state has no charges present and the total electric field is l_0 on each link. Hence, the total energy $E_{l_0<l_0^*}$ is just the electric field energy

$$E_{l_0<l_0^*} = a(N-1)g^2 \frac{l_0^2}{2}, \tag{7}$$

where we have made use of the fact that on a lattice with open boundaries we have $N-1$ links. On the right of the phase transition ($l_0 > l_0^*$), the ground state has a negative charge at the left edge of the system and a positive one at the right edge, connected by an electric flux string lowering total electric field by one unit. This results in a total electric field of $l_0 - 1$ on each link, and the total energy consists of the electric field energy plus a mass energy of $2m_r$ from the two charges

$$E_{l_0>l_0^*} = a(N-1)g^2 \frac{(l_0-1)^2}{2} + 2m_r. \tag{8}$$

These two energies become equal at $l_0 = l_0^*$, and solving for l_0^* by equating Eq. (7) with Eq. (8) we find

$$l_0^* = 2\frac{m_\mathrm{r}}{g}\frac{\sqrt{x}}{N-1} + \frac{1}{2}. \tag{9}$$

In the limit of large N, Eq. (9) becomes

$$l_0^* \approx 2\frac{m_\mathrm{r}}{g}\frac{\sqrt{x}}{N} + \frac{1}{2}, \tag{10}$$

where $\frac{\sqrt{x}}{N}$ is the dimensionless inverse volume. Hence, in the limit of infinite volume, we obtain the continuum prediction $l_0^* = 1/2$ as expected. If we now take again Eq. (9) and insert for the volume $N/\sqrt{x} = 30$, and express the renormalized mass in terms of the lattice mass and a mass shift (MS), we arrive at the result

$$l_0^* = 2\left(\frac{m_\mathrm{lat}}{g} + \mathrm{MS}\right)\frac{1}{30 - ag} + \frac{1}{2}. \tag{11}$$

The mass shift decreases with decreasing ag [1, 9]. Further, the factor $1/(30 - ag)$ decreases as $ag \to 0$, which leads to an overall decrease of the first term and Eq. (11) tends towards the continuum limit. Hence, we see that the transition point on finite lattices l_0^* is generally shifted towards values larger than $1/2$ and gets closer to the continuum theory prediction for decreasing lattice spacing.

As a further exemplification of Eq. (9) using staggered fermions, we show in Fig. 5 the behaviour of the phase transition point l_0^* as a function of $1/N$ for $x = 7, 9$, which allows us to remain above dimensionless physical volumes of 30. Without loss of generality, we choose a small renormalized mass at $m_\mathrm{r}/g = 0.5$ near the second order phase transition point which will have a value of l_0^* close to 0.5 according to Eq. (9) and then double that renormalized mass at $m_\mathrm{r}/g = 1$. To find l_0^* for each value of $N, x, m_\mathrm{r}/g$, we use the bisection method [10] with the EFD observable by first finding the ground state as an MPS. The variational algorithm to find the ground states stops when the relative change in energy is less than 10^{-11} and we set the bond dimension limit high enough such that the cutoff on the singular values of 10^{-15} does not saturate the bond dimension. Hence, we can consider the error from neglecting singular values with magnitude less than 10^{-15} negligible. Any l_0 giving a positive EFD value is considered to be less than l_0^* and vice versa. The algorithm will stop when the left and right l_0 values have a distance of 10^{-9}. For each value of l_0, we compute the mass shift to keep a fixed renormalized mass throughout. To find the mass shift we again use the bisection method with the EFD observable. We start the algorithm for the mass shift with a left and right value of m_lat/g that we assume is to the left and right of where the EFD goes to 0. Through the sign of the EFD value, this gives directly a definition of which m_lat/g are to the left or right of the m_lat^*/g that represents minus the mass shift. We again stop the algorithm at a tolerance of 10^{-9}. From the data in Fig. 5 we can see that as m_r/g is decreased, the l_0^* gets closer to 0.5. Further, as x is increased the l_0^* increases but gives a steeper gradient. Finally, as N is increased the l_0^* decreases, all of which are expected by Eq. (9).

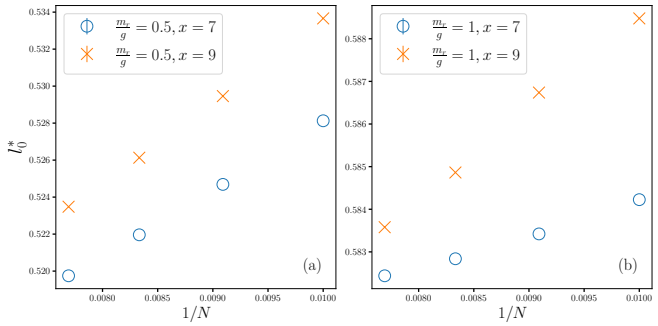

Supplementary Figure 5. The phase transition point l_0^* is shown against $1/N$ for $x = 7, 9$ and $m_\mathrm{r}/g = 0.5$ (a), 1 (b). The error bars on the individual points are approximated by the bisection method explained in the main text and are smaller than the y-scale, thus not visible.

[1] Angelides, T., Funcke, L., Jansen, K. & Kühn, S. Computing the mass shift of Wilson and staggered fermions in the lattice schwinger model with matrix product states. *Phys. Rev. D* **108**, 014516 (2023). URL https://link.aps.org/doi/10.1103/PhysRevD.108.014516.

[2] Zache, T. V. *et al.* Quantum simulation of lattice gauge theories using Wilson fermions. *Quantum Science and Technology* **3**, 034010 (2018). URL https://doi.org/10.1088/2058-9565/aac33b.

[3] Hamer, C. J., Weihong, Z. & Oitmaa, J. Series expansions for the massive Schwinger model in Hamiltonian lattice theory. *Phys. Rev. D* **56**, 55–67 (1997). URL https://link.aps.org/doi/10.1103/PhysRevD.56.55.

[4] Jordan, P. & Wigner, E. P. About the Pauli exclusion principle. *Z. Phys.* **47**, 631–651 (1928).

[5] Fishman, M., White, S. R. & Stoudenmire, E. M. The ITensor Software Library for Tensor Network Calculations. *SciPost Phys. Codebases* 4 (2022). URL https://scipost.org/10.21468/SciPostPhysCodeb.4.

[6] Haegeman, Jutho. Variational renormalization group methods for extended quantum systems. *Ghent University. Faculty of Sciences* XX, 354 (2011).

[7] Singh, S., Pfeifer, R. N. C. & Vidal, G. Tensor network decompositions in the presence of a global symmetry. *Phys. Rev. A* **82**, 050301 (2010). URL https://link.aps.org/doi/10.1103/PhysRevA.82.050301.

[8] Adam, C. Massive Schwinger Model within Mass Perturbation Theory. *Ann. Phys.* **259**, 1–63 (1997). URL https://www.sciencedirect.com/science/article/pii/S0003491697956979.

[9] Dempsey, R., Klebanov, I. R., Pufu, S. S. & Zan, B. Discrete chiral symmetry and mass shift in the lattice Hamiltonian approach to the Schwinger model. *Phys. Rev. Res.* **4**, 043133 (2022). URL https://link.aps.org/doi/10.1103/PhysRevResearch.4.043133.

[10] Burden, R. L. & Faires, D. J. *Numerical analysis* (PWS Publishing Company, Boston, 1985), 3 edn.